

Catalytic Effects of Zeolite Socony Mobil-5 (ZSM-5) on the Oxidation of Acoustically Levitated *exo*-Tetrahydrodicyclopentadiene (JP-10) Droplets

Sahan D. Perera, Stephen J. Brotton, Haylie Shinsato, Ralf I. Kaiser,* Yuyeol Choi, and Kyungsu Na*

Cite This: <https://doi.org/10.1021/acs.jpca.1c02892>

Read Online

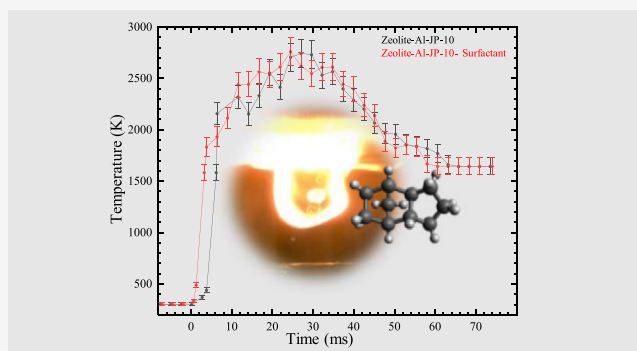
ACCESS |

Metrics & More

Article Recommendations

Supporting Information

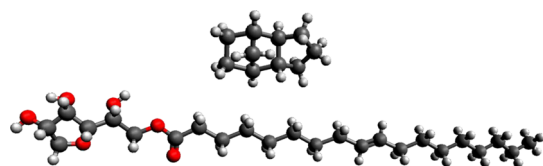
ABSTRACT: Jet propulsion 10 (JP-10) droplets with and without aluminum nanoparticles in conjunction with HZSM-5 zeolite and surfactants were ultrasonically levitated, and their oxidation processes were explored to identify how the oxidation process of JP-10 is catalytically affected by the HZSM-5 zeolites and how the surfactant and Al NPs in the system impacted the key experimental parameters of the ignition such as ignition delay time, burn rate, and the maximum temperatures. Singly levitated droplets were ignited using a carbon dioxide laser under an oxygen–argon atmosphere. Pure JP-10 droplets and JP-10 droplets with silicon dioxide of an identical size distribution as the zeolite HZSM-5 did not ignite in strong contrast to HZSM-5-doped droplets. Acidic sites were found to be critical in the ignition of the JP-10. With the addition of the surfactant, the characteristic features of the JP-10 ignition were improved, so the ignition delay time of the zeolite-JP-10 samples were decreased by 2–3 ms and the burn rates were increased by 1.3 to $1.6 \times 10^5 \text{ K s}^{-1}$. The addition of Al NPs increased the maximum temperatures during the combustion of the systems by 300–400 K. Intermediates and end products of the JP-10 oxidation over HZSM-5 were characterized by UV–vis emission and Fourier-transform infrared transmission spectroscopies, revealing key reactive intermediates (OH, CH, C₂, O₂, and HCO) along with the H₂O molecules in highly excited rovibrational states. Overall, this work revealed that acetic sites in HZSM-5 are critical in the catalytic ignition of JP-10 droplets with the addition of the surfactant and Al NPs, enhancing the oxidation process of JP-10 over HZSM-5 zeolites.



1. INTRODUCTION

Jet propulsion 10 (JP-10) represents one of the most promising synthetic hydrocarbon fuels exploited in military aircrafts due to its attractive thermophysical properties such as low freezing point, high specific impulse, and low viscosity.^{1–6} The *exo*-TCD (tricyclo[5.2.1.0^{2,6}] decane) or *exo*-tetrahydrodicyclopentadiene molecule (C₁₀H₁₆; Scheme 1) represents the principal constituent of JP-10; the strained polycyclic molecular structure of this hydrocarbon results in a high

Scheme 1. Molecular Structure of *exo*-Tetrahydrodicyclopentadiene (JP-10) (Top) and the Surfactant (Bottom)^a



^aCarbon, hydrogen, and oxygen atoms are color-coded in gray, white, and red, respectively.

volumetric energy of 39.6 kJ cm^{-3} .² Consequently, JP-10 is not only used as a high-energy density fuel for advance air-breathing propulsion systems but also utilized in the experimental and theoretical physical chemistry and material sciences communities to study key features in the fundamental decomposition and oxidation mechanism of ring-strained molecules. These studies are vital to build up efficient combustion models and to design proficient coolants along with chemical heat sinks for advanced aircraft and missile engines.^{7–13}

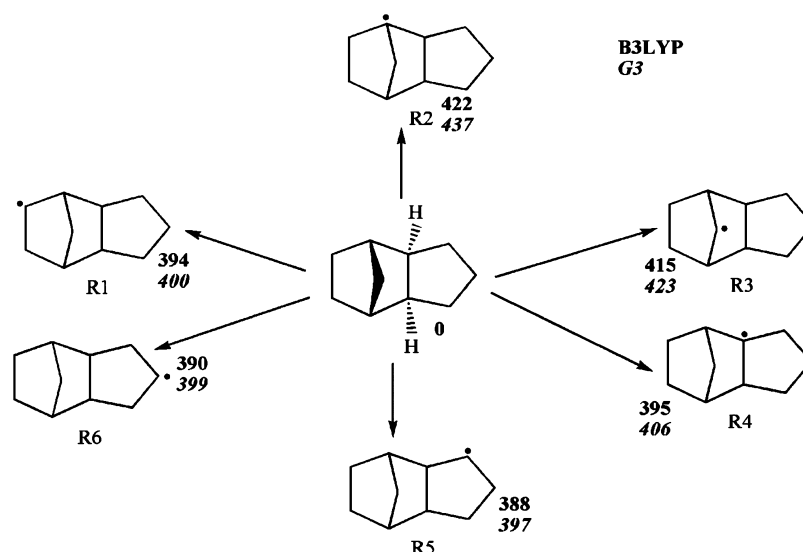
Over the past decades, researchers exploited a great variety of approaches to study the thermal decomposition and oxidation of JP-10 such as distinct reactor types (flow tube, jet stirred, and batch),^{11,14–20} shock tubes,^{2,7,21} and high-temperature chemical reactors (Table 1) with identified

Received: March 31, 2021

Revised: May 7, 2021

Table 1. Compilation of Prior Experimental Studies on the Pyrolysis of JP-10

method	temperature (K)	pressure (bar)	residence time (ms)	refs
vacuum ultraviolet photoionization (ALS/NSRL)	1100–1600/927–1083	0.8/1.101	a few 0.01/124–144	10
shock tube	1166–1522	2.53–3.04		24
electrically heated tube	823–1008	45		25
flow reactor with a fixed bed/microflow tube	673–733/700–980	60/1	6500–13,000/400	26
shock tube	1000–1600	6–8	0.5	7
flow tube reactor	298–1700	0.002–0.004	2.10–9.35	14
flow tubular reactor	930–1080	1.7	3.2–5.3	8
jet-stirred reactor	848–933	1	500–6000	16
annular tubular reactor	903–968			18
system for thermal diagnostic studies	373–873	34	1038–5000	23
system for thermal diagnostic studies	473–935	34	1800	1
batch reactor	823–903	1–38	480–26,400	19
tubular reactor	883–963	1	1.8×10^6	20
thermal block	623–698	345	2.4×10^5 , 7.2×10^7	3
batch reactor	583–683	40	3.6×10^7	17
flow reactor	900–1600	0.00667		15

Scheme 2. Radicals Generated via C–H Bond Cleavages in JP-10^{10a}

^aThe reaction energies for the CH bond ruptures were calculated at the B3LYP/6-311G** and G3 level and are given in kJ mol^{-1} .¹⁰

products compiled in Table S1.^{10,22,23} The majority of these products were reported in a chemical microreactor setup by Zhao et al.¹⁰ by exploiting vacuum ultraviolet photoionization detection along with studies by Johnson et al.,²⁴ Pan et al.,²⁵ and Huang et al.²⁶ Electronic structure calculations by Morozov et al.²² provided a theoretical framework of these findings and yielded in-depth mechanistical insights into the feasible pathways, leading to the pyrolysis products of JP-10. These studies revealed that the decomposition of JP-10 is initiated by distinct C–H bond cleavages^{10,22,24} followed by C–C bond β -scissions via biradical intermediates; these pathways are consistent with the cleavage of strained C–C bonds eventually initiating the unimolecular decomposition of the carbon skeleton of JP-10 (Scheme 2).²⁴ Zhao et al.¹⁰ revealed that R1, R4, R5, and R6 represent favorable channels due to the lower endoergicities of the C–H bond cleavages.^{10,22} Overall, the pyrolysis of JP-10 was found to be most efficient at temperatures exceeding 873 K due to the high activation energies of at least 397 kJ mol^{-1} to cleave the carbon–hydrogen bond(s) (Scheme 2).^{10,14–17,20,21}

Distinct catalysts have been proposed to decrease the activation energy in the decomposition of JP-10. Li et al.²⁷ explored the effects of gold nanoparticles, but the improvement of the cracking rate of JP-10 only achieved 10% with the dispersion stability of metal nanoparticles, limiting the use as a catalyst in JP-10 decomposition. On the other hand, zeolites—microporous, aluminosilicate minerals—have emerged as potentially effective catalysts in the decomposition and also oxidation of JP-10 due to their high catalytic activity, thermal stability, cation exchange capability, shape selectivity, and effective acidic sites in their structural framework.^{13,28–30} The catalytic activity of zeolites critically depends on multiple factors such as the aluminum content in terms of the silicon dioxide (SiO_2) to aluminum oxide (Al_2O_3) ratio of the zeolite framework,^{13,31–35} the type of cation (H^+ , Na^+ , K^+ , and Li^+) exchange in the aluminum framework,^{32,36} the pore size,^{13,35,37} the particle size³⁸ of the zeolite, and also the moisture level.³⁹ Particular attention has been devoted to Zeolite Socony Mobil 5 (ZSM-5)—a Mobil five (MFI) type of zeolite, where its framework is formed by bonding multiple pentasil units.^{37,40}

This structure creates 10-membered ring micropores of 0.51 to 0.56 nm in diameter.⁴¹ In general, zeolite frameworks are solely microporous in nature, but distinct ZSM-5 structures with both micropores and mesopores such as NaZSM-5, HZSM-5, and HZSM-5 nanosheets can be synthesized with a mesopore diameter of 2 to 50 nm.^{13,33,37} These dimensions can be compared to the JP-10 molecule holding a maximum diameter of 0.67 nm and a minimum diameter of 0.38 nm.^{10,42} The pores create straight and sinusoidal channels throughout the structure and allow molecules such as JP-10 to diffuse and to react with interior surface sites, which leads to the catalytic decomposition of JP-10. The smallest diameter of JP-10 of 0.38 nm allows diffusion into the micropore channels (0.51–0.56 nm) of ZSM-5, but the diffusion is limited for the 0.67 nm diameter JP-10; however, the larger mesopores (2–50 nm) would easily allow all JP-10 molecules to diffuse through. Therefore, JP-10 is thought to react preferentially with the acidic sites of the mesopores.^{13,34,35}

Extensive research exists from the material science community on the cracking of JP-10 in the presence of these zeolites. Due to the limited space in this journal, only key findings will be reported, which are important to place the present experiments into context. Xing et al.³⁴ examined the decomposition and oxidation of JP-10 over ZSM-5 in the temperature ranges from 773 to 873 K; the authors revealed that cracking rates of JP-10 improved by more than 45% compared to non-catalyzed thermal cracking with major products reported in Table S2. Hence, ZSM-5 catalysts have outstanding performance in catalytic cracking and oxidation of JP-10 due to the robust open silica structure,⁴³ ideal pore size,^{13,35} and number of catalytic acidic sites in the ZSM-5 framework.^{13,35} However, unwanted side effects such as the deactivation of the zeolite catalyst by coke formation and dealumination processes during the decomposition and oxidation of JP-10 have not been solved yet.^{32,44–46} Xing et al.³⁴ reported that a fundamental limiting factor for the catalytic cracking of JP-10 was the number of acidic sites available on the external surfaces of HZSM-5.³⁴ Multiple studies have suggested that the initial reaction of JP-10 and the first β -scission of the JP-10 carbenium ions proceed with the acidic sites on the external surfaces of the ZSM-5.^{13,34} Unless in the gas phase, where radical intermediates are formed, ionic intermediates likely dominate the catalytic decomposition in the presence of zeolites. The β -scission of the JP-10 carbenium ions usually occurs along with excessive isomerization. The primary products then undergo further secondary reactions within the zeolitic pores on the internal acidic sites. Tian et al.³⁵ completed a study to minimize the limitations of the micropores by turning HZSM-5 into nanosheets.³⁵ The majority of the acid sites were located on the internal surfaces of the zeolite, which limited the JP-10 catalytic cracking rate. The purpose of creating the HZSM-5 nanosheets was to create mesopores with more external acidic sites and shorter diffusion paths to enhance the catalytic activity. This provided more mesopores with accessible external acidic sites, which increased the catalytic activity of the initial reaction of JP-10 molecules and carbenium ions. The same catalytic cracking products as observed by Xing et al.³⁴ were revealed with the HZSM-5 nanosheets, with the addition of butane, butene, pentane, and pentene.^{34,35} The product distribution observed from the nanosheets was slightly different from the normal HZSM-5 in that there was a decrease in gaseous products (methane, ethane, propane, and butane). Tian et al.³⁵ attributed the

difference to the shorter diffusion paths that resulted in less secondary reactions and hydrogen shifts due to the limited amount of time products and reactants within the channels.

Kim et al.¹³ compared the catalytic activities and properties of various zeolites (HBEA, HY, HMOR, HFER, and HZSM-5) by studying the catalytic cracking of JP-10 and ZSM-5 that showed the highest catalytic activity among all other zeolites by providing the highest C1–C4 product yield. Here, the comparison is based on the C1–C4 product yield due to several reasons. Methane (CH₄), ethane (C₂H₆), ethene (C₂H₄), propane (C₃H₈), propylene (C₃H₆), and butane (C₄H₁₀) were the dominant gaseous products formed during the catalytic oxidation of JP-10 over zeolite.¹³ HZSM-5 was revealed to yield the highest yields of C1–C4 hydrocarbons, while HFER—a catalyst with the smallest micropore diameter of 0.42 nm—produced the lowest amount of C1–C4 products, thus demonstrating the critical role of the pore sizes and diffusion-limited decomposition in the catalytic activity of zeolites. The remaining zeolites explored (HBEA, HY, and HMOR) had larger micropore diameters (0.65, 0.78, and 0.66 nm) than HZSM-5 (0.56 nm) but yielded smaller amounts of C1–C4.¹³ These results are also supported by the product distributions observed by Huang et al.²⁶ in the catalytic cracking of JP-10 over HY zeolite. The product distribution observed by the HY zeolite was similar to the HZSM-5 product distribution; however, the majority of the HY zeolite products were C5 products [cyclopentadiene (C₅H₁₀) and cyclopentene (C₅H₈)] rather than C1–C4 products. This could be attributed to the larger pore sizes of HBEA, HY, and HMOR that allowed for a quicker rate of diffusion, resulting in less time for the primary products to undergo catalytic cracking reactions that produce C1–C4. Overall, the micropore diameter of HZSM-5 revealed to be the ideal size out of all the zeolites for the production of C1–C4 products. Kim et al.¹³ also observed that JP-10 with HZSM-5 produced higher amounts of acyclic hydrocarbons and aromatics than with other catalysts due to the narrow channels that provided more time for the primary decomposition products to react with the acidic sites available.

Despite the aforementioned progress in understanding the catalytic activities in the decomposition of JP-10 in the presence of zeolite catalysts, concerns on the limited volumetric energy density of JP-10 of only 40 kJ cm⁻³, which severely constrain the range and hence performance of air-breathing propulsion systems, are growing. The development of the next generation of air-breathing propulsion systems requires fuel with higher energy per volume and molecular weight compared to traditional hydrocarbon fuel. This necessitates the next generation of high-energy-density fuel and of high-energy-density fuel additives, ultimately enhancing the performance and range of air-breathing propulsion systems. Aluminum nanopowder (Al NP) high-energy-density fuel additives hold promising applications in air breathing engine applications.^{47–52} Having high energy density (84 kJ cm⁻³) and higher surface-area-to-volume ratio, aluminum nanoparticles significantly improve the JP-10 ignition delay, increase the maximum flame temperatures, and reveal a rapid burning rate of JP-10.^{47,49,53–57} However, there is currently an incomplete understanding of the underlying mechanisms involved in the decomposition and oxidation of metal-doped JP-10-based fuel, in particular, in the presence of zeolites. To our best knowledge, no experimental work has been conducted on the oxidation of Al NPs in the

presence of JP-10 over HZSM-5 catalysts. Therefore, the objectives of the present work are to investigate the catalytic oxidation of JP-10 (system a) over HZSM-5 first as a reference system and then in the presence of added Al NPs (system b) exploiting an ultrasonic levitation apparatus.⁵⁸ We further explore the effects of adding the surfactant (Span 80) to the JP-10-zeolite (system c) and JP-10-zeolite-Al NP (system d) on the oxidation of JP-10.

2. EXPERIMENTAL METHODS

2.1. Materials. JP-10 ($C_{10}H_{16}$, $\geq 98\%$ pure Scheme 1), AlNPs (nominal diameter of 80 nm, 99.99%), and the sorbitane monooleate surfactant ($C_{24}H_{44}O_6$ -span 80, ≤ 60 Scheme 1) were purchased from BOC Science, Novacentrix, and Sigma-Aldrich, respectively, and were used without further purification. The zeolites samples (HZSM-5) were synthesized in house. Briefly, MFI zeolites were synthesized hydrothermally using a Teflon-lined autoclave. Aluminum isopropoxide ($C_9H_{21}O_3Al$, $\geq 98\%$, Sigma-Aldrich) and tetraethylorthosilicate ($SiC_8H_{20}O_4$ -TEOS, 98%, TCI) are used as aluminum (Al) and silica (SiO_2) precursors, respectively. Tetrapropylammonium hydroxide ($C_{12}H_{29}NO$ -TPAOH, 40% solution in water, Sigma-Aldrich) was used as the micropore-directing agent. The molar composition of the synthesis gel was $9TPAOH/xAl_2O_3/25SiO_2/495H_2O/100C_2H_5OH$, where x is varied among 0 and 0.5. In a typical synthesis, 35.42 g of TPAOH and 20.07 g of C_2H_5OH were dissolved in 10.29 g of distilled water. Into this solution, a desired amount of $C_9H_{21}O_3Al$ was added under vigorous stirring until the solution became transparent. After that, 23.15 g of TEOS was added dropwise, and the resultant solution was stirred for 24 h at room temperature. The final gel was transferred to a Teflon-lined autoclave, which was hydrothermally treated at 413 K for 48 h. After the hydrothermal synthesis, the solution was cooled down to room temperature, and the precipitate was collected by filtration, dried in an oven at 373 K, and calcined at 773 K for 4 h under air condition. Except the purely siliceous sample (silicalite-1), the aluminum-containing zeolite sample was further ion-exchanged to the protonated form with 1 M ammonium nitrate solution (NH_4NO_3) three times. The molar amount of NH_4NO_3 in the ion-exchange solution was 10 times larger than the molar amount of aluminum in the zeolite framework. Each ion-exchange process was carried out for 2 h at room temperature. After the ion-exchange process, the zeolite samples were calcined at 773 K for 4 h under air conditions to form proton-exchanged zeolite. Hereafter, the purely siliceous sample and H^+ -exchanged zeolite samples are named silicalite-1 and HZSM-5, respectively.

2.2. Sample Preparation. Four distinct JP-10 samples were prepared by mixing JP-10 with (a) 5 wt % HZSM-5 zeolite (zeolite-JP-10), (b) 5 wt % HZSM-5 zeolite and 1 wt % Al NPs (zeolite-Al-JP-10), (c) 1 wt % HZSM-5 zeolite and span 80 (zeolite-JP-10-surfactant), and (d) 1 wt % HZSM-5 zeolite, 1 wt % Al NPs, and span 80 (zeolite-Al-JP-10-surfactant). Levitated droplets are shown in Figure 1. It is important to note that without the surfactant, the HZSM-5 zeolite did not disperse uniformly within JP-10. Therefore, samples (a) and (b) required high concentrations (5 wt %) of the zeolite in order to transfer zeolite particles into the levitated JP-10 droplets. In contrast, in the presence of the surfactant, particle agglomeration of both Al NPs and HZSM-5 zeolites was eliminated, and the nanoparticles and zeolite were uniformly distributed in JP-10 at a concentration of as low as 1

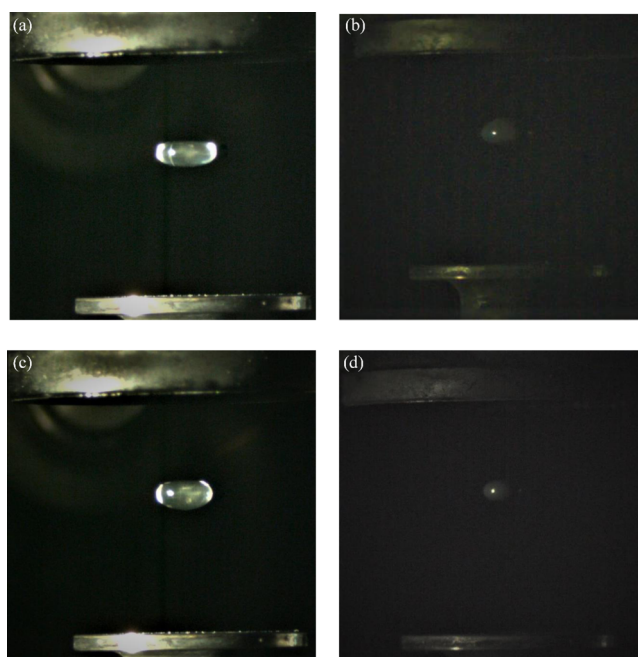


Figure 1. Optical images of levitated droplets of JP-10 containing (a) 5 wt % HZSM-5 zeolites (hereafter, zeolite-JP-10), (b) 5 wt % HZSM-5 zeolites and 1 wt % Al NPs (hereafter, zeolite-Al-JP-10), (c) 1 wt % HZSM-5 zeolites and 5 wt % span 80 (hereafter, zeolite-JP-10-surfactant), and (d) 1 wt % HZSM-5 zeolites, 1 wt % Al NPs, and 5 wt % span 80 (hereafter, zeolite-Al-JP-10-surfactant).

wt %. All samples were sonicated (Branson 3510:115 V AC, 10 min) to ensure that no separation between the particles and the liquid takes place during the experiments. As reference systems, samples of JP-10 with silicalite-1, that is, pure silicon dioxide, of an identical size distribution as HZSM-5 were also prepared for the study. However, the silicalite-1/JP-10 samples did not ignite at all. This behavior was expected since the acidity of the silicalite-1 is very low compared to the HZSM-5 sample (Figure 2, Table 2). With the insufficient acidic sites within the silicalite-1 surfaces, the catalytic activity of the initial reaction of JP-10 molecules and carbenium ions will be restricted. As a result, the reactive intermediates which initiate the ignition process of JP-10 will not be formed with the silicalite-1/JP-10 samples. Therefore, silicalite-1/JP-10 samples did not ignite at all.

2.3. Material Characterization for Zeolite Samples.

Wide-angle X-ray powder diffraction patterns were obtained on a Rigaku MiniFlex 600 diffractometer using $Cu K\alpha$ radiation in the 2θ range of 5 and 50°. The morphology of the zeolites was identified by scanning electron microscopy (SEM, Gemini 500), operated with an accelerating voltage of 1 kV. From the SEM images, histograms of average size distributions of zeolite crystals were constructed by counting 100 of zeolite particles with ImageJ software. Nitrogen adsorption and desorption isotherms were measured using ASAP 2020 (Micromeritics) at liquid nitrogen temperature. Prior to the measurements, the samples were degassed under vacuum at 573 K for 3 h. The surface area of the powders was analyzed with the Brunauer–Emmett–Teller (BET) method. The Si/Al ratio was obtained using inductively coupled plasma optimal emission spectroscopy (ICP-OES, PerkinElmer, OPTIMA 8300). The acidity of zeolite samples was analyzed by the temperature-programmed desorption equipped with mass detector (TPD-MS) technique

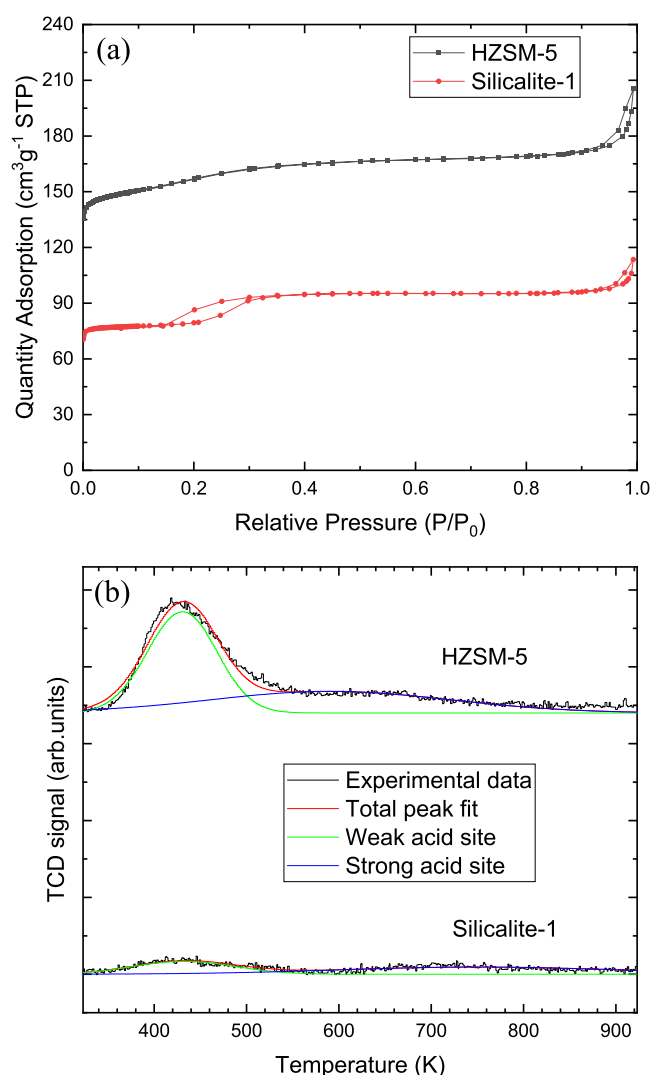


Figure 2. (a) Nitrogen (N_2) adsorption isotherms and (b) ammonia (NH_3) TPD-MS profiles of H^+ -MFI-65 (hereafter, HZSM-5) and MFI- ∞ (hereafter, silicalite-1). The ammonia TPD profiles can be deconvoluted to three peaks: total peak fit (red), weak (green), and strong (blue) acidic sites. The nitrogen adsorption isotherm of HZSM-5 was offset by $50 \text{ cm}^3 \text{ g}^{-1}$.

with a BEL-CAT (Bel Japan Inc.). Prior to the measurement, all the zeolite samples were preheated with helium (He) for 2 h to degas adsorbed molecules. Preheated samples were cooled down to 323 K, at which ammonia (NH_3) was adsorbed on the zeolite surface using 5 wt % NH_3/He gas flow for 1 h. After then, samples were purged with He gas for 0.5 h and stabilized for 1 h. The desorption process was carried out under helium flow with a ramping rate of 10 K min^{-1} .

Table 2. Physicochemical Properties of Zeolite Samples

name	Si/Al ratio ^a	average crystal size ^b (nm)	S_{BET} ^c ($\text{m}^2 \text{ g}^{-1}$)	V_{tot} ^d ($\text{cm}^3 \text{ g}^{-1}$)	acidity ^e (mmol g^{-1})		
					total	weak	strong
HZSM-5	65	218 ± 22	339	0.26	0.035	0.020	0.015
silicalite-1	∞	216 ± 18	308	0.19	0.010	0.006	0.004

^aSi/Al ratio determined by ICP-OES. ^bAverage crystal size determined by SEM images in Figure 4. ^c S_{BET} , BET surface area calculated by BET theory. ^d V_{tot} total pore volume calculated at $P/P_0 = 0.95$ by BJH theory using the adsorption branch of N_2 adsorption isotherm in Figure 2a. ^eAmount of acidic sites determined by NH_3 TPD-MS in Figure 2b.

2.4. Acoustic Levitation Apparatus and Characterization Techniques. The oxidation of singly levitated JP-10 droplets in the presence of zeolite was examined by exploiting an ultrasonic levitator. The detailed description of this device can be found in earlier publications.^{49,58–60} In brief, the levitator consists of a piezoelectric transducer at an oscillation frequency of 58 kHz and a concave shape reflector. A standing wave is generated from the reflection of the ultrasonic sound waves between the transducer and the reflector; the acoustic radiation pressure counterbalances the gravitational force and hence levitates the droplet slightly below one of the pressure nodes of the standing wave. This ultrasonic levitator is implemented into a pressure-compatible stainless-steel process chamber, so the levitated droplet can be studied in different gas(eous) environments (inert, toxic, and/or reactive). In the current study, the droplets were levitated in an environment of 60% oxygen (O_2 , 99.9999%, Airgas) and 40% argon (Ar, 99.9999%, Airgas) at a total pressure of 936 ± 1 Torr to overcome the minimum ignition conditions of the present droplets.⁴⁹ The droplets were oblate spheroids in shape with mean horizontal and vertical diameters of 2.4 ± 0.3 and 1.4 ± 0.2 mm, respectively (Figure 1). The droplets were introduced into the pressure node with the help of a homemade droplet deposition system.⁵⁸ This unit consists of a microneedle, a wobble stick, polyetheretherketone tubing, and a syringe. The levitated droplets were then heated using a carbon dioxide (CO_2) laser emitting at a wavelength of $10.6 \mu\text{m}$. The laser output can be tuned in between 1 and 40 W; the present work was performed at an output power of 32 W, which is achieved by setting the duty cycle of the CO_2 laser to 80%; this laser power overcame the minimum ignition conditions of the present droplets.⁴⁹

The ignition process of JP-10 in the presence of the zeolite samples was characterized using ultraviolet–visible (UV–vis) and Fourier-transform infrared (FTIR) spectroscopies along with an IR thermal-imaging and a high-speed optical camera. Raman spectroscopy of the droplets was attempted, but the spectra exhibited a smooth structureless continuum with no discrete peaks. Reactive intermediates, atoms, and closed-shell molecules including terminal oxidation products produced during the oxidation were detected via UV–vis emission spectroscopy in emission and through FTIR. UV–vis spectra were recorded via a StellarNet SILVER-Nova UV–vis spectrometer by exploiting a fiber optic probe covering the wavelength range of 200–1100 nm with a spectral resolution of 2 nm. The UV–vis spectra of the JP-10-zeolite samples before ignition were recorded via the same UV spectrometer but exploiting a Hamamatsu L10290 UV–vis fiber light source and Y-type fiber-optic reflectance probe.⁶⁰ FTIR transmission spectra were recorded with the help of a Nicolet 6700 FTIR spectrometer over the wavelength range of $500\text{--}5000 \text{ cm}^{-1}$ to detect gases evolved during the ignition event. Time scales of

fuel ignitions are short, typically in the order of a few tens of milliseconds.^{9,47,49,61} Therefore, optical videos of these high-speed events were captured by a Phantom Miro 3a10 camera (Supporting Information; [Movies M1](#) and [M2](#)) with a Navitar Zoom 6000 modular lens system at a rate of 1000 frames per second (fps). Additionally, thermal-imaging videos of the ignition process were acquired by the FLIR A6703sc infrared camera; this assists in the examination of important features in the combustion process such as ignition delay, maximum flame temperature (T_{\max}), and burn rate. In this work, thermal-imaging videos were acquired over six temperature ranges of 283–363, 353–473, 423–623, 523–873, 773–1473, and 973–1773 K at a frame rate of 387.55 s^{-1} . The thermal-imaging videos of the highest three temperature ranges were acquired with an ND2 filter. In order to enhance the statistical accuracy for the ignition process of JP-10-HZSM-5 samples, each temperature range was duplicated by five separate ignition events, so a total of 30 videos were acquired for the full temperature range. The videos of each temperature range were then converted to temporal plots of the maximum temperature using the FLIR ResearchIR Max program. Consequently, temporal profiles of each temperature range were combined in order to obtain a single temperature temporal profile for the full range of observed temperatures. Finally, the temperatures above the autoignition of JP-10 (509 K)^{3,9,47} were calibrated in the temperature temporal profile by extracting the emissivity of the flame.⁴⁷

3. RESULTS

3.1. Crystallinity and Acidity of the Zeolite Samples.

The crystallinities of different zeolite samples were analyzed by X-ray diffraction (XRD). As shown in [Figure 3](#), all the zeolite

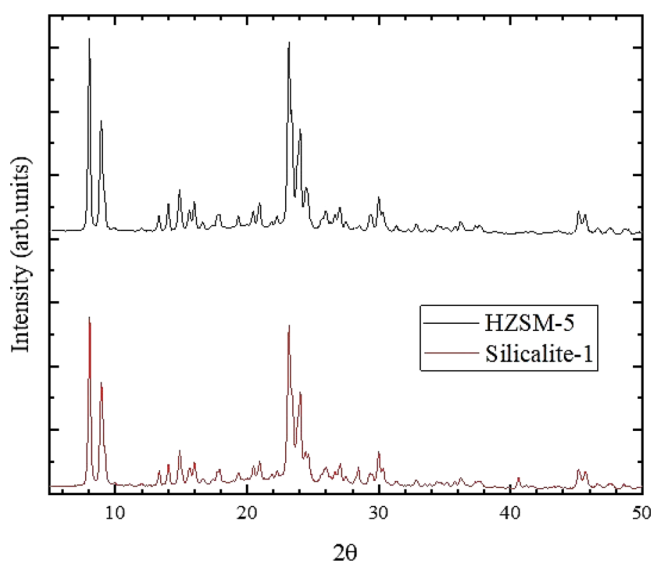


Figure 3. XRD patterns of HZSM-5 and silicalite-1.

samples exhibited similar XRD patterns that corresponded to the typical reflections of the zeolite framework (JCPDS 42-0023).⁶² Very sharp XRD reflections indicate that the individual crystalline domains were well-faceted and single-crystalline. In fact, the suggested crystalline morphology was confirmed by SEM. As visualized in [Figure 4](#), the zeolite samples exhibited a typical coffin-shaped morphology with very uniform size and shape. The individual zeolite crystals are

single-crystalline with smooth and well-faceted surfaces. The average sizes of two zeolite samples were obtained using ImageJ software exploiting an average of about 100 particles. As revealed in the histograms in [Figure 4](#), two zeolite samples were obtained as very similar crystal sizes between 200 and 250 nm. The average sizes of HZSM-5 and silicalite-1 were calculated as 218 and 216 nm, respectively ([Table 2](#)). The XRD and SEM investigations confirmed that the two zeolite samples were successfully synthesized into the same framework type of crystalline MFI structure with very uniform size and shape of individual zeolite particles. The porosity of zeolite samples was characterized with nitrogen (N_2) adsorption isotherms, which confirmed a typical characteristic adsorption phenomenon of the microporous crystal ([Figure 2](#)). The two samples are solely microporous. The BET surface areas and total pore volumes are not significantly different from each other ([Table 2](#)). Contrary to other textural properties, the acidity of the zeolite samples was distinct due to the difference of aluminum content in the framework. As shown in ammonia (NH_3) TPD-MS profiles in [Figure 2b](#), the HZSM-5 desorbed ammonia according to the increase in desorption temperature, whereas the silicalite-1 sample showed a negligible ammonia TPD profile. Due to the purely siliceous framework of the silicalite-1 sample, no appreciable acidic sites existed in the zeolite framework.

3.2. Temperature Profiles. [Figure 5](#) compiles the temporal temperature profiles for the ignition of zeolite-JP-10 ([Figure 5a](#)) and zeolite-Al-JP-10 droplets ([Figure 5b](#)) with and without the span 80 surfactant. For both zeolite-JP-10 and zeolite-Al-JP-10 droplets, characteristic ignition features such as the ignition delay time were improved with the addition of the surfactant. In the preignition stage, zeolite-JP-10 required 5 ms to reach the autoignition temperature of JP-10 of 509 K,^{3,9,47} whereas the addition of span 80 reduced this time by 2 to 3 ms ([Figure 5a](#)). A similar reduction was observed for zeolite-Al-JP-10 droplets without and with surfactants reaching the autoignition temperature after 4 ms and only 1 ms, respectively. Overall, adding the surfactant decreased the ignition delay time of the samples by 2 to 3 ms. It shall be stressed that for the zeolite-JP-10 and zeolite-Al-JP-10 systems, 40 and 76% of the droplets ignited, respectively. This increased to 70 and 100% with the addition of the surfactant, demonstrating superior ignition statistics in the experiments. After the autoignition, in the second state of the oxidation process, a rapid temperature increase occurred with maximum rates of $2.6 \pm 0.4 \times 10^5$ and $4.3 \pm 0.3 \times 10^5 \text{ K s}^{-1}$ for zeolite-JP-10 without and with the surfactant, respectively ([Figure 5a](#)). Similarly, the zeolite-Al-JP-10 systems without and with the surfactant revealed maximum rates of $3.5 \pm 0.3 \times 10^5$ and $4.8 \pm 0.3 \times 10^5 \text{ K s}^{-1}$, respectively. Therefore, the burn rate of both the zeolite-JP-10 and zeolite-Al-JP-10 samples slightly improved with the addition of the surfactant. In the third stage, the droplet ignited, and the temperature increased more slowly compared to the second stage, reaching a maximum value (T_{\max}) after typically 25 to 30 ms, except for the zeolite-JP-10 system without the surfactant; the latter reached T_{\max} much slower due to weak dispersion of HZSM-5 zeolite within JP-10. Consequently, the catalytic oxidation and maximum temperature of zeolite-JP-10 significantly improved with the addition of the surfactant. For each system, average T_{\max} temperatures were obtained as follows

$$T_{\max}(\text{zeolite-JP-10}) = 2240 \pm 102 \text{ K} \quad (1)$$

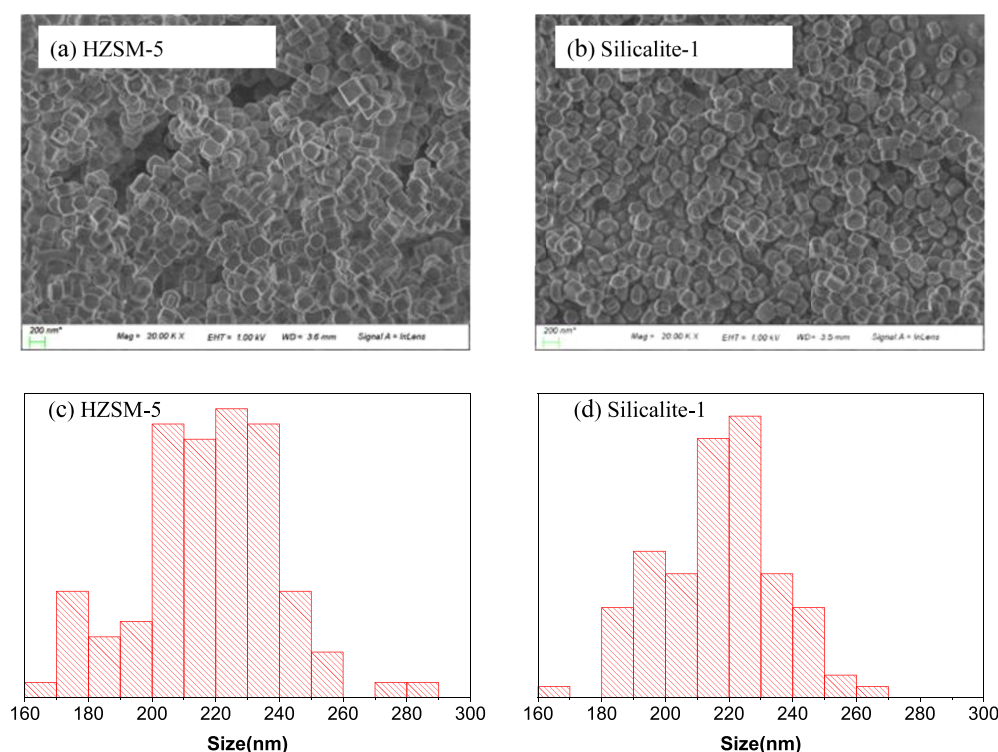


Figure 4. SEM images of (a) HZSM-5 and (b) silicalite-1 and (c,d) their respective histograms.

$$T_{\max}(\text{zeolite-JP-10-surfactant}) = 2380 \pm 108 \text{ K} \quad (2)$$

$$T_{\max}(\text{zeolite-Al-JP-10}) = 2620 \pm 107 \text{ K} \quad (3)$$

$$T_{\max}(\text{zeolite-Al-JP-10-surfactant}) = 2627 \pm 116 \text{ K} \quad (4)$$

within the error limits, the addition of the surfactant does not change the maximum ignition temperature for the zeolite-JP-10 and zeolite-Al-JP-10 systems. However, the addition of aluminum nanoparticles systematically increases T_{\max} by 300 to 400 K by considering the higher energy density and enhanced energy release in the oxidation process. Once the systems reach T_{\max} , the temperatures decrease as the fuel is consumed. At the end after about 60 ms, the droplet falls out of the trap and drops on the transducer.⁶³ Since our goal is to study the combustion of the levitated droplet, the temperature fluctuations occurring by the splash ignition are neither shown in Figure 5 nor discussed.

3.3. UV–Vis Emission Spectroscopy. Figures 6 and 7 compare the UV–vis emission spectra for the ignition of zeolite-JP-10 (Figure 6) and zeolite-Al-JP-10 droplets (Figure 7) without (a) and with (b) surfactants. A black-body spectrum was fitted to the UV–vis raw data and obtained flame temperatures of $2307 \pm 60 \text{ K}$ (zeolite-JP-10), $2223 \pm 70 \text{ K}$ (zeolite-JP-10-surfactant), $2225 \pm 70 \text{ K}$ (zeolite-Al-JP-10), and $2200 \pm 65 \text{ K}$ (zeolite-Al-JP-10-surfactant). The spectral features in the UV–vis emission spectra of all four systems reveal that the atoms, molecules, and radicals generated from the JP-10 ignition are similar in each system. Hence, the contribution from the flame emission to the blackbody background should be similar, so all four systems exhibited similar flame temperatures within the error limits. However, with the addition of the surfactant, relative intensities of the bands especially in the 300 to 500 nm wavelength range increased (Figures 6b and 7b). The band centers and assignments for the observed peaks in the UV–vis emission

spectra of the systems are compiled in Tables 3 and 4. The observed UV–vis peaks and band centers exhibited a closer agreement with the published literature.^{47,64–69} Here, the UV–vis emission spectra are dominated by hydroxyl (OH), methylidyne (CH), diatomic carbon (C_2), molecular oxygen (O_2), and formyl (HCO) in the range of 300–580 nm.⁶⁴ The OH (289–310 and 340–360 nm) and CH ($\sim 390 \text{ nm}$) emissions represented the $\text{A}^2\Sigma^+ - \text{X}^2\Pi$ and $\text{A}^2\Delta - \text{X}^2\Pi$ transitions, respectively.^{64,65} The shoulder peak (330–340 nm) next to the OH could be due to the emissions of the O_2 or HCO which represented the $\text{B}^3\Sigma_u^- - \text{X}^3\Sigma_g^-$ and $\tilde{\text{A}}^2\text{A}'' - \tilde{\text{X}}^2\text{A}'$ transitions, respectively.^{64,70} Both O_2 and HCO transitions are appeared at the same wavelength ($\sim 337 \text{ nm}$),^{64,70} so it was difficult to separate. The C_2 swan bands at 612 nm are defined through the $\text{d}^3\Pi_g - \text{a}^3\Pi_u$ transition.^{64,65} In the zeolite sample, replacement of silicon by aluminum causes a cation charge deficiency; this deficiency is compensated not only by protons (H^+) but also by sodium (Na^+) and potassium (K^+)^{32,36} Hence, in the present work, we also observed strong Na and K emissions centered around 589 and 767 nm. In addition, highly excited rotational–vibrational modes of water (H_2O) appeared as broad bands throughout the UV–vis emission spectra (600–900 nm).⁶⁹ Water is also evident through the broad emissions from 900 to 1000 nm.⁶⁷ It is also noted that the UV–vis emission spectra of the zeolite-Al-JP-10 droplets did not show any significant peaks for aluminum monoxide (AlO)—the dominating diatomic species formed in the oxidation of aluminum.^{47,48} This could be due to the lower flame temperatures observed for the zeolite-Al-JP-10 samples (2200 K) versus 2690 K for systems without the zeolites,⁴⁷ thus eliminating any chemiluminescence of AlO. The spectral comparison of the UV–vis reflectance spectra are compiled in the Supporting Information (Figures S1 and S2). No discrete reflectance peaks are evident from zeolite or aluminum. Since more than 95% by weight of the droplet contained JP-10, the

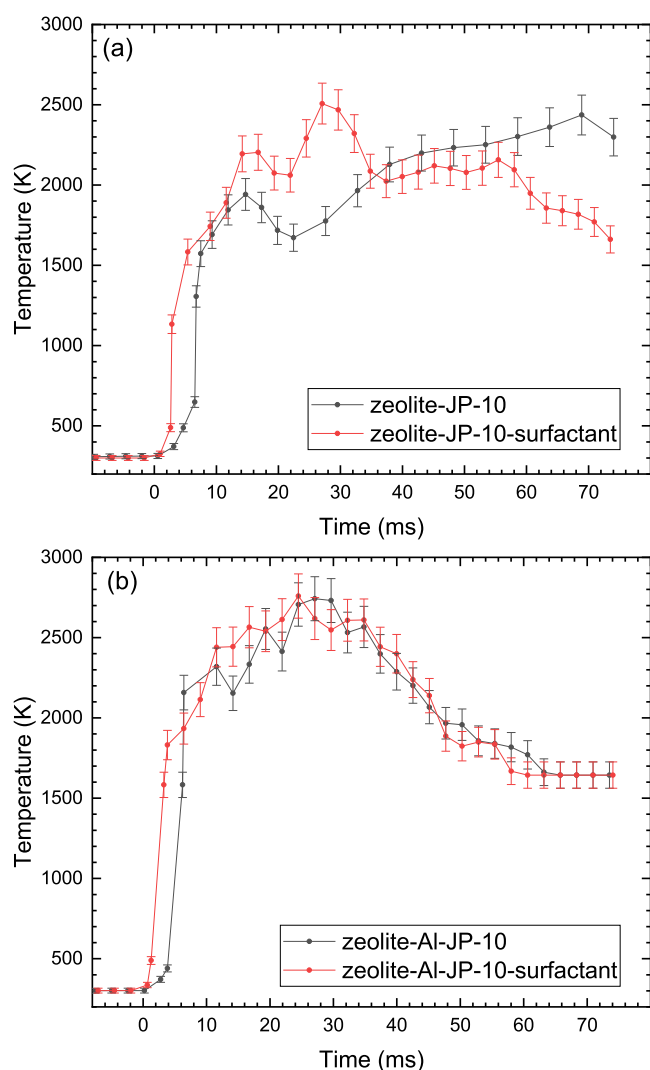


Figure 5. Temperature temporal profiles produced by igniting droplets of (a) zeolite-JP-10 and zeolite-JP-10-surfactant and (b) zeolite-Al-JP-10 and zeolite-Al-JP-10-surfactant. The laser irradiation started at $t = 0$ s.

concentrations of the zeolite and aluminum were insufficient to generate any distinct features in UV–vis reflectance spectroscopy.

3.4. FTIR Spectroscopy. Figure 8 shows the FTIR transmission spectrum following ignition of a zeolite-JP-10-surfactant droplet. The IR data collected after the complete combustion of the droplet captured the gaseous products of the oxidation. The absorption features of the combustion products and evaporated JP-10 were labeled (a–k) in Figure 8 and are tabulated in Table 5. The final products of the oxidation of JP-10, carbon dioxide (CO_2), and water (H_2O) were detected by the FTIR measurements. The observed band/peaks of the vibrational modes of CO_2 ,^{66,71,72} H_2O ,⁶⁶ and unreacted JP-10⁴⁸ exhibited a close agreement with the published literature. The FTIR transmission spectra of the oxidation products of all four systems revealed similar features, so the FTIR spectra of the remaining three systems are presented in the Supporting Information (Figures S3–S5, Tables S3–S5).

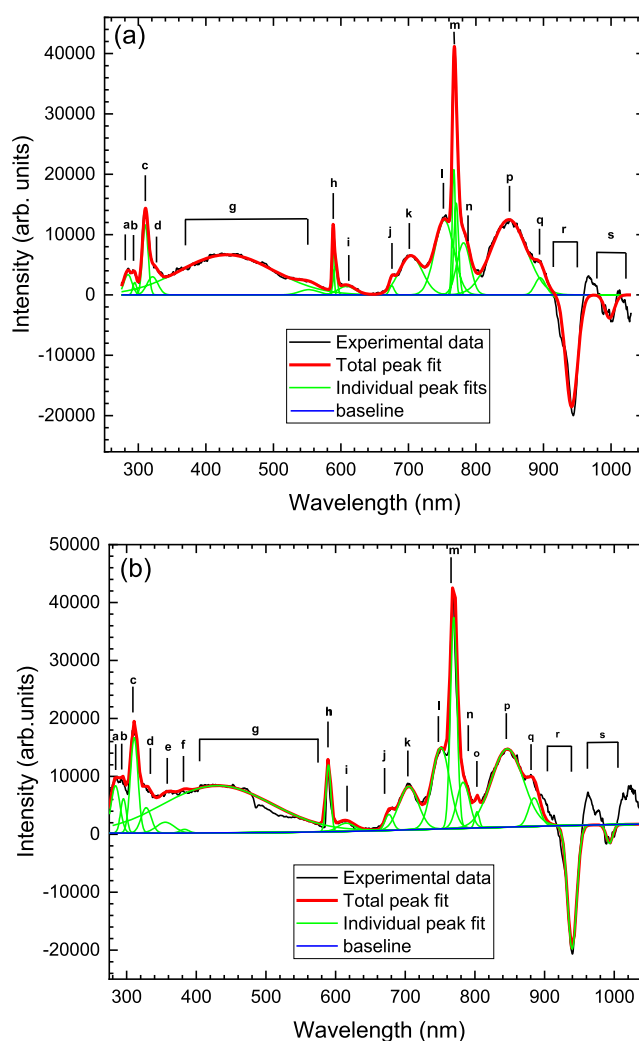


Figure 6. UV–vis emission spectrum produced during ignition of droplets of (a) zeolite-JP-10 and (b) zeolite-JP-10-surfactant. The total fit (red line) was obtained by simultaneously optimizing a black-body background and Gaussian peaks (green lines) across the 270–1100 nm wavelength range. Here, the black-body background of (a) 2307 ± 60 and (b) 2223 ± 70 K has been subtracted to show the emission peaks and bands more clearly. The assignments of bands a–s are presented in Table 3.

4. DISCUSSION

Our experiments yielded the following key results which are compiled and discussed below:

- (1) JP-10 droplets did not ignite in the absence of HZSM-5; hence, the presence of HZSM-5 is critical to the ignition process and the inherent mechanism.
- (2) JP-10 droplets with pure silicon dioxide (silicalite-1) of identical size distributions as HZSM-5 did not ignite. Therefore, the presence of acidic sites in the HZSM-5 zeolite is critical to the ignition process and to the underlying mechanism.
- (3) The addition of aluminum nanoparticles to the zeolite-JP-10 systems increased the maximum temperature (T_{max}) by 300 to 400 K.
- (4) Adding the surfactant to the zeolite-JP-10 and zeolite-Al-JP-10 systems decreased the ignition delay time by 2 to 3 ms; it further increased the burn rate of the JP-10 by 1.3

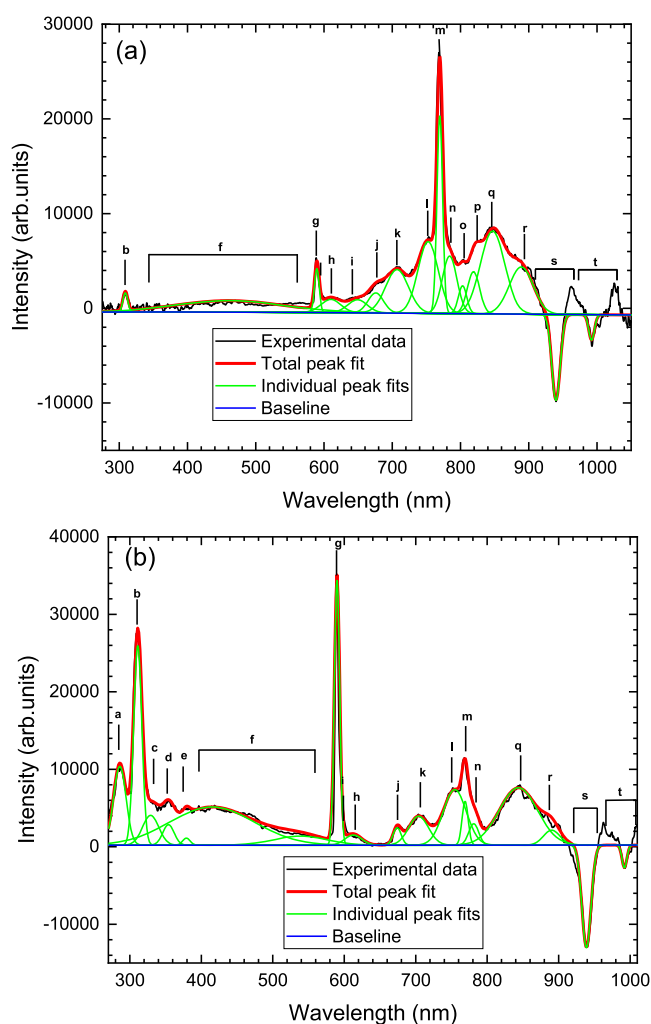


Figure 7. UV-vis emission spectrum produced during ignition of droplets of (a) zeolite-Al-JP-10 and (b) zeolite-Al-JP-10-surfactant. The total fit (red line) was obtained by simultaneously optimizing a black-body background and Gaussian peaks (green lines) across the 270–1100 nm wavelength range. Here, the black-body background of (a) 2225 ± 70 and (b) 2200 ± 65 K has been subtracted to show the emission peaks and bands more clearly. The assignments of bands are presented in Table 4.

to 1.6×10^5 K s^{-1} ; overall, the characteristic features of the JP-10 ignition were improved.

- (5) The UV-vis emission measurements revealed the dominance of OH, C₂, CH, O₂, and HCO radicals along with highly excited rotational-vibrational modes of H₂O.
- (6) The FTIR data revealed the “terminal” gas-phase oxidation products of JP-10, that is, CO₂ and H₂O.

First, the temperature temporal profiles were exploited to characterize the ignition features (ignition delay time, burning rates, and T_{\max}) in the zeolite-JP-10 samples (systems a–d); the addition of the surfactant to the zeolite-JP-10 and zeolite-Al-JP-10 systems critically improved the ignition features of JP-10, as evidenced in Figure 5. These findings may help to acquire an understanding on the catalytic cracking and oxidation mechanism of JP-10 over HZSM-5 to explain the experimental trends.^{31,33–35,73} In order to ignite JP-10 in the presence of the zeolite, JP-10 molecules must be able to diffuse to the acidic sites within the HZSM-5 zeolite surfaces. For this

to happen, the molecular diameter of JP-10 (0.38–0.67 nm)^{10,42} and pore size of HZSM-5 must allow diffusion. Therefore, the diffusion rate of JP-10 is strictly controlled by the pore size of HZSM-5.^{34,35} The zeolite (HZSM-5) used in this work is solely microporous with a pore diameter ranging from 0.51 to 0.56 nm,^{33,37} so JP-10 can only diffuse with its elongated dimension parallel into micropore channels; diffusion is limited by the 0.67 nm diameter of JP-10. Also, due to the absence of mesopore channels (2–50 nm diameter) in the zeolite framework, decomposition of JP-10 is most likely controlled by the acidic sites located on the outer surfaces of the micropores.^{35,73} For this reason, the zeolite-JP-10 system (system a) exhibited a slower ignition rate and it took more time to reach the T_{\max} (Figure 5a). However, with the addition of the surfactant, the particle agglomeration was mostly eliminated (Section 2.2)^{55,74} and the diffusion rate of JP-10 into HZSM-5 was improved;⁵⁵ this likely increased the ability of individual JP-10 molecules to interact with the acidic sites within the zeolite. As a result, ignition properties (burning rate and ignition delay time) of zeolite-JP-10 droplets (systems c and d) were improved with the addition of the surfactant (Figure 5).

Once the ignition started (Figure 5), zeolite-JP-10 samples (systems a and c) showed a slight temperature drop at higher temperatures ($T > 1600$ K) compared to the zeolite-Al-JP-10 samples (systems b and d). This is possibly due to the greater stability of the HZSM-5 catalytic structure^{31,33} in zeolite-Al-JP-10 samples (systems b and d) at higher temperatures. The Si–O–X–Al (X = Na, H, and K) moiety in the zeolite framework represents an essential structure to retain the catalyst stability and efficiency during the ignition process of JP-10,³² but the stability of this moiety is greatly affected by the dealumination process; this process has been shown to occur at temperatures as low as 700 K.^{31,33} However, with the presence of Al NPs in the JP-10-zeolite droplets, the dealumination process in the zeolite framework can be slowed down;³² hence, the presence of Al NPs may improve the zeolite’s catalytic stability at higher temperatures. In addition to this, Al has excellent heat conductivity; this allows heat to distribute quickly within the zeolite-Al-JP-10 droplet. Therefore, unlike zeolite-JP-10 samples, zeolite-Al-JP-10 samples exhibited a steady temperature increase at higher temperatures (Figure 5b). Finally, the T_{\max} values of the temperature temporal profiles of zeolite-Al-JP-10 samples were significantly higher than the zeolite-JP-10 samples. This is mostly due to the high energy density (84 kJ cm^{-3}) and high surface-area-to-volume ratio of the Al NPs present in zeolite-JP-10 samples.^{47,49}

Second, in the present work, reactive intermediates, individual atoms, and final oxidation products produced by the catalytic oxidation of JP-10 over HZSM-5 were identified by UV-vis emission spectroscopy and FTIR spectroscopy (Figures 6–8). However, before discussing the emission features in the UV-vis emission spectra (Figures 6 and 7) of zeolite-JP-10 systems (systems a–d), it is important to understand how these emission lines and bands are generated in Figures 6 and 7. For example, emissions resulting in the C₂ feature at 613 nm, with the corresponding excitation energy, E , of 3.24×10^{-19} J, require a temperature, E/k_b , of 2.3×10^4 K (where k_b is the Boltzmann constant). In the present work, the highest temperatures achieved (flame temperatures) by the UV-vis emission spectra were around 2200 K, which is a factor of about 10 lower than the temperature required (2.3×10^4 K). Therefore, the emission lines in the UV-vis spectra

Table 3. Vibrational Mode Assignments for the Peaks or Bands in the UV–Vis Emission Spectrum of Droplets of Zeolite-JP-10 and Zeolite-JP-10-Surfactant

peak or band	peak wavelength or band center (nm) ^a zeolite	peak wavelength or band center (nm) ^a zeolite-span80	molecule, atom, or radical	ref wavelength (nm)	transition	branch; vibrational quantum numbers: (ν' , ν'') or (ν'_1, ν'_2, ν'_3)–($\nu''_1, \nu''_2, \nu''_3$)
a	286.5	286.5	OH	287.5–289.3 ^b	$A^2\Sigma^+ - X^2\Pi$	R ₁ , R ₂ , Q ₁ , Q ₂ ; (2,1)
b	289.5	289.5	OH	287.5–289.3 ^b	$A^2\Sigma^+ - X^2\Pi$	R ₁ , R ₂ , Q ₁ , Q ₂ ; (2,1)
c	309.5	309.5	OH	309.0 ^b	$A^2\Sigma^+ - X^2\Pi$	Q ₂ ; (0,0)
d	336.5	336.5	O ₂	337.0 ^b	$B^3\Sigma_u^- - X^3\Sigma_g^-$	(0,14)
			HCO	337.6 ^{b,i}	$\tilde{A}^2A'' - \tilde{X}^2A'$	
e		354.5	OH	342–359 ^{b,c}	$A^2\Sigma^+ - X^2\Pi$	(1,0), (2,1)
f		389.0	CH	390.0 ^{b,c}	$A^2\Delta - X^2\Pi$	(0,0)
g	300–580 (broad)	300–580 (broad)	OH, C ₂ , CH	ref ^b		
h	589.0	589.0	Na	589.59 ^d	$^2S_{1/2} - ^2P_{3/2}$	
				589.00 ^d	$^2S_{1/2} - ^2P_{1/2}$	
i	613.5	613.0	C ₂	612.2 ^b	$d^3\Pi_g - a^3\Pi_u$	(1,3)
j	678.1	676.1	H ₂ O	632–683 ^e	ro-vib. mode	(1,1,3)–(1,5,1)
k	701.5	701.5	H ₂ O	690–710 ^f	ro-vib. mode	(1,0,3)–(0,0,0)
l	753.5	753.5	H ₂ O	719–795 ^e	ro-vib. mode	(1,2,2)–(0,1,3)
m	767.5	767.5	K	767.50 ^{d,g}	$^2S_{1/2} - ^2P_{3/2}$	
				769.90 ^{d,g}	$^2S_{1/2} - ^2P_{1/2}$	
n	781.0	788.0	H ₂ O	719–795 ^e	ro-vib. mode	(1,2,2)–(0,1,3)
o		802.5	H ₂ O	719–795 ^e	ro-vib. mode	(1,2,2)–(0,1,3)
p	849.5	849.5	H ₂ O	847–906 ^e	ro-vib. mode	(0,0,3)–(1,3,1)
q	892.5	883.5	H ₂ O	847–906 ^e	ro-vib. mode	(0,0,3)–(1,3,1)
r	944.5 opt. fiber. absorp. ^h	944.5 opt. fiber. absorp. ^h	H ₂ O ^f	928–966 ^f ref ^h	ro-vib. mode	(2,0,1)–(0,0,0)
s	998.5	998.5	H ₂ O	972–1017 ^{e,h}	ro-vib. mode	(2,2,0)–(0,4,1)

^aMeasurements are accurate to within 2 nm. ^bReference 59. ^cReference 60. ^dReference 61. ^eReference 64. ^fReference 62. ^gReference 63. ^hReference 46. ⁱReference 65.

Table 4. Vibrational Mode Assignments for the Peaks or Bands in the UV–Vis Emission Spectrum of Droplets of Zeolite-Al-JP-10 and Zeolite-Al-JP-10-Surfactant

peak or band	peak wavelength or band center (nm) ^a zeolite-Al-JP-10	peak wavelength or band center (nm) ^a zeolite-Al-JP-10-span80	molecule, atom, or radical	ref wavelength (nm)	transition	branch; vibrational quantum numbers: (ν' , ν'') or (ν'_1, ν'_2, ν'_3)–($\nu''_1, \nu''_2, \nu''_3$)
A		288.5	OH	287.5–289.3 ^b	$A^2\Sigma^+ - X^2\Pi$	R ₁ , R ₂ , Q ₁ , Q ₂ ; (2,1)
B	309.5	309.5	OH	309.0 ^b	$A^2\Sigma^+ - X^2\Pi$	Q ₂ ; (0,0)
C		337.1	O ₂	337.0 ^b	$B^3\Sigma_u^- - X^3\Sigma_g^-$	(0,14)
			HCO	337.6 ^{b,i}	$\tilde{A}^2A'' - \tilde{X}^2A'$	
D		355.0	OH	342–359 ^{b,c}	$A^2\Sigma^+ - X^2\Pi$	(1,0), (2,1)
E		388.5	C–H	390.0 ^{b,c}	$A^2\Delta - X^2\Pi$	(0,0)
F	300–580 (broad)	300–580 (broad)	OH, C ₂ , CH	ref ^b		
G	589.5	589.0	Na	589.59 ^d	$^2S_{1/2} - ^2P_{3/2}$	
				589.00 ^d	$^2S_{1/2} - ^2P_{1/2}$	
H	612.5	613.0	C ₂	612.2 ^b	$d^3\Pi_g - a^3\Pi_u$	(1,3)
I	642.5		H ₂ O	632–683 ^e	ro-vib. mode	(1,1,3)–(1,5,1)
J	678.5	678.1	H ₂ O	632–683 ^e	ro-vib. mode	(1,1,3)–(1,5,1)
K	702.5	708.0	H ₂ O	690–710 ^f	ro-vib. mode	(1,0,3)–(0,0,0)
l	753.5	752.5	H ₂ O	719–795 ^e	ro-vib. mode	(1,2,2)–(0,1,3)
m	769.5	769.5	K	767.50 ^{f,g}	$^2S_{1/2} - ^2P_{3/2}$	
				769.90 ^{f,g}	$^2S_{1/2} - ^2P_{1/2}$	
n	778.0	778.0	H ₂ O	719–795 ^e	ro-vib. mode	(1,2,2)–(0,1,3)
o	802.5		H ₂ O	719–795 ^e	ro-vib. mode	(1,2,2)–(0,1,3)
p	832.5		H ₂ O	811–839 ^e	ro-vib. mode	(2,1,1)–(0,0,0)
q	847.5	847.5	H ₂ O	847–906 ^e	ro-vib. mode	(0,0,3)–(1,3,1)
r	888.5	888.5	H ₂ O	847–906 ^e	ro-vib. mode	(0,0,3)–(1,3,1)
s	944.5 opt. fiber. absorp. ^h	944.5 opt. fiber. absorp. ^h	H ₂ O ^f	928–966 ^f ref ^h	ro-vib. mode	(2,0,1)–(0,0,0)
t	998.5	998.5	H ₂ O	972–1017 ^{e,h}	ro-vib. mode	(2,2,0)–(0,4,1)

^aMeasurements are accurate to within 2 nm. ^bReference 59. ^cReference 60. ^dReference 61. ^eReference 64. ^fReference 62. ^gReference 63. ^hReference 46. ⁱReference 65.

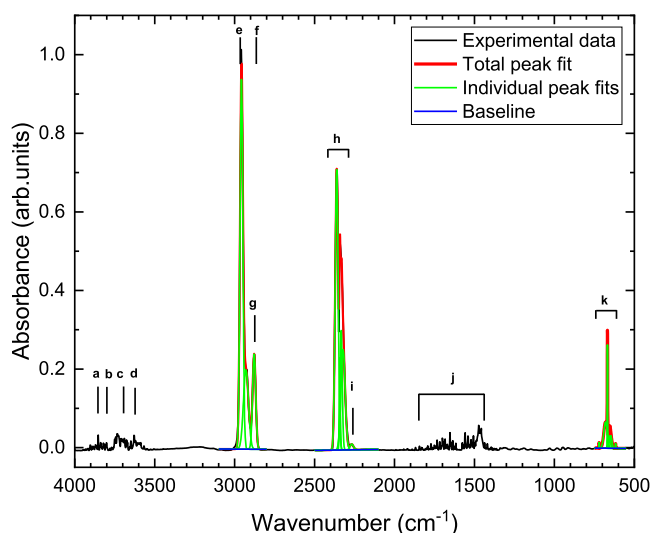
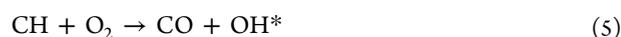


Figure 8. FTIR transmission spectrum following ignition of droplets of the zeolite-JP-10-surfactant. The rovibrational peaks/bands of the products and unreacted JP-10 are labeled (a–k) and assigned in Table 5. The total fit (red line) and individual peak fit peaks (green lines) are shown. FTIR transmission spectra of other three systems are shown in the Supporting Information.

were not caused by heat, but the emissions of the intermediates and products were the result of electronically excited states formed through chemical reactions (chemiluminescence). In Figure 7, UV–vis emission spectra of zeolite-Al-JP-10 systems (systems b and d) did not show any significant peaks for the dominating diatomic species (AlO) formed in the oxidation of aluminum,^{47,48} thus, all four zeolite systems (systems a–d) behaved similar to each other. The absence of AlO peaks in the zeolite-Al-JP-10 systems could be due to two reasons. One is the lower flame temperatures observed for the zeolite-Al-JP-10 samples (2200 K) versus 2690 K for systems without the zeolites.^{47,48} The lower flame temperatures in zeolite-Al-JP-10 samples are possibly due to the deactivation of the zeolite catalyst by coke formation and dealumination processes during the decomposition and oxidation of JP-10. An alternative

possibility could be the involvement of AlO in the dealumination process of the zeolite framework to slow down the dealumination rate at higher temperatures (Figure 5b).³² This could also make aluminum oxide species unavailable for chemiluminescence at a given temperature. Therefore, the emission features of the zeolite-JP-10 samples in Figures 6 and 7 can be discussed based on the three regions of the UV–vis emission spectra (200–600, 600–900, and 900–1100 nm). In the wavelength region from 200 to 600 nm, the OH, CH, O₂, HCO, and C₂ radicals dominated the UV–vis emission spectra of zeolite-JP-10 samples (systems a–d). These radicals are the characteristic features of the UV–vis emission spectra of hydrocarbon flames,⁶⁴ and these excited species can be formed via the following possible chemical reactions.^{64,75}

OH



where * denotes an electronically excited state.

C₂



where the atomic carbon is most likely produced by



CH



These radicals were actively involved in the decomposition process of JP-10 and formed a variety of primary and secondary decomposition products listed in Table S2.^{34,35} The spectral features observed in the 600–900 nm region were dominated by the emission bands from H₂O molecules in highly excited ro-vibrational states.^{67,69}

H₂O



These features were supported by measurements of H₂O vapor at temperatures of around 2500 K, which also produced similar overall broad features to present work in the same wavelength region.^{67,69} Here, each feature represents different

Table 5. Vibrational Mode Assignments for the Peaks or Bands in the FTIR Transmission Spectrum of Droplets of Zeolite-JP-10

band	peak or band wavenumber ^a (cm ⁻¹)	molecule	ref band (cm ⁻¹)	number (symmetry)	vibrational mode ^b
a	3756	H ₂ O	3756 ^c	3(b ₁)	$\nu_{\text{as}}(\text{H}_2\text{O})$
b	3714	CO ₂	3714.8 ^d	1(σ_{g}^+) + 3(σ_{u}^+)	combination band
c	3657	H ₂ O	3657 ^c	1(a ₁)	$\nu(\text{H}_2\text{O})$
d	3612	CO ₂	3612.8 ^d	1(σ_{g}^+) + 3(σ_{u}^+)	combination band
e	2956	C ₁₀ H ₁₆	2942 ^e	68	$\nu(\text{CH})$
f	2929	C ₁₀ H ₁₆	2913 ^e	62	$\nu(\text{CH}_2)$
g	2879	C ₁₀ H ₁₆	2865 ^e	57	$\nu(\text{CH})$
h	2347	CO ₂	2349.1 ^d	3(σ_{u}^+)	$\nu_{\text{as}}(\text{CO}_2)$
	2359	CO ₂	2300–2380 ^f		$\nu_{\text{as}}(\text{CO}_2)$
i	2279	¹³ C ¹⁶ O ₂	2283 ^e	3(σ_{u}^+)	$\nu_{\text{as}}(\text{CO}_2)$
j	1600	H ₂ O	1595 ^c	2(a ₁)	$\delta(\text{OH})$
	1457	C ₁₀ H ₁₆	1456 ^e	54	scissoring (CH ₂)
	1466	C ₁₀ H ₁₆	1468 ^e	55	scissoring (CH ₂)
k	668	CO ₂	667.4 ^d	2(π_{u})	$\delta(\text{CO}_2)$
	648	¹³ C ¹⁶ O ₂	649.0 ^e	2(π_{u})	$\delta(\text{CO}_2)$
	619, 655, 680, 720	CO ₂	620–710 ^f	2(π_{u})	$\delta(\text{CO}_2)$

^aSpectral resolution of 4 cm⁻¹. ^b ν denotes stretch; bend; and as, antisymmetric. ^cReference 61. ^dReference 66. ^eReference 47. ^fReference 67.

combination bands of water, so they were labeled (ν_1, ν_2, ν_3) in Tables 4 and 5, where ν_1, ν_2 , and ν_3 represented the O–H symmetrical stretch, the H–O–H bend, and the O–H asymmetric stretch of water molecule, respectively.⁶⁷ Similarly, the broad absorption region from 900 to 1000 nm closely represented the different combination bands of H₂O vapor, but the spectral interpretation was complicated by the absorption from the optical fiber in the same wavelength region.

Finally, spectral features in the FTIR transmission spectra (Figures 8 and S3–S5) reveal the standard end products of the hydrocarbon (JP-10) oxidation.



Thus, CO₂ and H₂O and unreacted JP-10 are found to be the end products of the catalytic oxidation of JP-10 over HZSM-5 zeolite systems (systems a–d).

5. CONCLUSIONS

We acoustically levitated JP-10 droplets with and without aluminum nanoparticles in conjunction with HZSM-5 zeolite and surfactants (systems a–d) exploiting a levitator experimental setup. The singly levitated droplets were ignited using a carbon dioxide laser under an oxygen–argon atmosphere; the oxidation processes were characterized using FTIR and UV–vis spectroscopies along with infrared thermal imaging and high-speed optical cameras. The objective of this work was to identify how the oxidation process of JP-10 is catalytically affected by the HZSM-5 zeolites and how the surfactant and Al NPs in the system impacted the key experimental parameters of the ignition such as the ignition delay time, burn rate, and maximum temperatures. Overall, pure JP-10 droplets and JP-10 droplets with silicalite-1 of an identical size distribution as HZSM-5 did not ignite in strong contrast to the HZSM-5-doped droplet. Consequently, the acidic sites present in the HZSM-5 zeolite are critical in the ignition of the JP-10 droplets. With the addition of the surfactant, the characteristic features of the JP-10 ignition were improved, so the ignition delay time of the zeolite-JP-10 samples was decreased by 2–3 ms and the burn rates were increased by 1.3 to 1.6 × 10⁵ K s⁻¹. Besides improving the ignition delay time and burn rates, the addition of Al NPs increased the maximum temperatures during the combustion of the systems by 300–400 K. Furthermore, intermediates and end products of the JP-10 oxidation over HZSM-5 were characterized by UV–vis emission and FTIR transmission spectroscopies. The UV–vis emission spectra revealed key reactive intermediates (OH, CH, C₂, O₂, and HCO) formed during the catalytic oxidation process of JP-10 over the zeolite along with the H₂O molecules in highly excited rovibrational states. The strong Na and K atomic emissions in the UV–vis measurements confirmed that the charge deficiency caused by the aluminum in the HZSM-5 zeolite framework is compensated by protons and monovalent cations: sodium and potassium. The FTIR measurements revealed CO₂ and H₂O as terminal gaseous products during the oxidation of JP-10 over HZSM-5 zeolites. Overall, this work showed that the HZSM-5 zeolite is critical in the ignition of JP-10 droplets with the addition of the surfactant and Al NPs, causing a positive impact to the oxidation process of JP-10 over HZSM-5 zeolite systems (systems a–d).

■ ASSOCIATED CONTENT

Supporting Information

The Supporting Information is available free of charge at <https://pubs.acs.org/doi/10.1021/acs.jpca.1c02892>.

UV–vis reflectance spectral comparison between the droplet of zeolite-JP-10, zeolite-aluminum-JP-10, and pure JP-10; UV–vis reflectance spectral comparison between the droplet of zeolite-span 80-JP-10, zeolite-aluminum-span 80-JP-10, and span 80-JP-10; FTIR transmission spectra following ignition of a JP-10 droplet containing zeolite, JP-10 droplet containing zeolite and aluminum NPs, and JP-10 droplet containing zeolite, aluminum NPs, and span 80; thermal decomposition products reported in the preceding experimental studies on JP-10; catalytic decomposition products reported in the preceding experimental studies on JP-10 over HZSM-5 zeolite; and vibrational mode assignments for the bands in the FTIR transmission spectrum of the JP-10 droplet containing zeolite, JP-10 droplet containing zeolite and aluminum NPs, and JP-10 droplet containing zeolite, aluminum NPs, and span 80 (PDF)

Optical high-speed video of the ignition of the JP-10 droplet containing zeolite and span 80 (MP4)

Optical high-speed video of the ignition of the JP-10 droplet containing zeolite, aluminum NPs, and span 80 (MP4)

■ AUTHOR INFORMATION

Corresponding Authors

Ralf I. Kaiser – Department of Chemistry, University of Hawaii at Manoa, Honolulu, Hawaii 96822, United States; orcid.org/0000-0002-7233-7206; Email: ralfk@hawaii.edu

Kyungsu Na – Department of Chemistry, Chonnam National University, Gwangju 61186, South Korea; orcid.org/0000-0001-5591-449X; Email: kyungsu_na@chonnam.ac.kr

Authors

Sahan D. Perera – Department of Chemistry, University of Hawaii at Manoa, Honolulu, Hawaii 96822, United States; orcid.org/0000-0002-4577-9025

Stephen J. Brotton – Department of Chemistry, University of Hawaii at Manoa, Honolulu, Hawaii 96822, United States

Haylie Shinsato – Department of Chemistry, University of Hawaii at Manoa, Honolulu, Hawaii 96822, United States

Yuyeol Choi – Department of Chemistry, Chonnam National University, Gwangju 61186, South Korea

Complete contact information is available at: <https://pubs.acs.org/10.1021/acs.jpca.1c02892>

Notes

The authors declare no competing financial interest.

■ ACKNOWLEDGMENTS

The Hawaii group was supported by the Office of Naval Research (ONR) under the contract number N000141912083. The synthesis of the zeolites was supported by the National Research Foundation of Korea (NRF) funded by the Ministry of Science and ICT (MSIT) [NRF-2021R1A2C2008362].

REFERENCES

- (1) Wohlwend, K.; Maurice, L. Q.; Edwards, T.; Striebich, R. C.; Vangness, M.; Hill, A. S. Thermal Stability of Energetic Hydrocarbon Fuels for Use in Combined Cycle Engines. *J. Propul. Power* **2001**, *17*, 1258–1262.
- (2) Davidson, D.; Horning, D.; Oehlschlaeger, M.; Hanson, R. The Decomposition Products of JP-10. *37th Joint Propulsion Conference and Exhibit*, 2012.
- (3) Bruno, T. J.; Bruno, T. J.; Huber, M. L.; Laesecke, A.; Lemmon, E. W.; Perkins, R. A. *Thermochemical and Thermophysical Properties of JP-10*; US Department of Commerce, National Institute of Standards and Technology, 2006; Vol. 6640, pp 1–66.
- (4) Colket, M. B.; Spadaccini, L. J. Scramjet Fuels Autoignition Study. *J. Propul. Power* **2001**, *17*, 315–323.
- (5) Chung, H. S.; Chen, C. S. H.; Kremer, R. A.; Boulton, J. R.; Burdette, G. W. Recent Developments in High-Energy Density Liquid Hydrocarbon Fuels. *Energy Fuels* **1999**, *13*, 641–649.
- (6) Osmont, A.; Gökalp, I.; Catoire, L. Evaluating Missile Fuels. *Propellants, Explos., Pyrotech.* **2006**, *31*, 343–354.
- (7) Gao, C. W.; Vandeputte, A. G.; Yee, N. W.; Green, W. H.; Bonomi, R. E.; Magoon, G. R.; Wong, H.-W.; Oluwole, O. O.; Lewis, D. K.; Vandewiele, N. M.; et al. JP-10 Combustion Studied with Shock Tube Experiments and Modeled with Automatic Reaction Mechanism Generation. *Combust. Flame* **2015**, *162*, 3115–3129.
- (8) Vandewiele, N. M.; Magoon, G. R.; Van Geem, K. M.; Reyniers, M.-F.; Green, W. H.; Marin, G. B. Kinetic Modeling of Jet Propellant-10 Pyrolysis. *Energy Fuels* **2015**, *29*, 413–427.
- (9) Parsinejad, F.; Arcari, C.; Metghalchi, H. Flame Structure and Burning Speed of JP-10 Mixtures. *Combust. Sci. Technol.* **2006**, *178*, 975–1000.
- (10) Zhao, L.; Yang, T.; Kaiser, R. I.; Troy, T. P.; Xu, B.; Ahmed, M.; Alarcon, J.; Belisario-Lara, D.; Mebel, A. M.; Zhang, Y.; et al. A Vacuum Ultraviolet Photoionization Study on High-Temperature Decomposition of JP-10 (exo-tetrahydrodicyclopentadiene). *Phys. Chem. Chem. Phys.* **2017**, *19*, 15780–15807.
- (11) Park, S. H.; Kwon, C. H.; Kim, J.; Han, J. S.; Jeong, B. H.; Han, H.; Kim, S. H. Mechanistic Insights Into Oxidative Decomposition of Exo-Tetrahydrodicyclopentadiene. *J. Phys. Chem. C* **2013**, *117*, 15933–15939.
- (12) Li, S. C.; Varatharajan, B.; Williams, F. A. Chemistry of JP-10 Ignition. *AIAA J.* **2001**, *39*, 2351–2356.
- (13) Kim, J.; Hyeon, D. H.; Park, S. H.; Chun, B.-H.; Jeong, B. H.; Han, J. S.; Kim, S. H. Catalytic Endothermic Reactions of Exo-Tetrahydrodicyclopentadiene with Zeolites and Improvement of Heat of Reactions. *Catal. Today* **2014**, *232*, 63–68.
- (14) Nakra, S.; Green, R. J.; Anderson, S. L. Thermal Decomposition of JP-10 Studied by Micro-Flowtube Pyrolysis-Mass Spectrometry. *Combust. Flame* **2006**, *144*, 662–674.
- (15) Li, H.; Liu, G.; Jiang, R.; Wang, L.; Zhang, X. Experimental and Kinetic Modeling Study of exo-TCDD Pyrolysis under Low Pressure. *Combust. Flame* **2015**, *162*, 2177–2190.
- (16) Herbinet, O.; Sirjean, B.; Bounaceur, R.; Fournet, R.; Battin-Leclerc, F.; Scacchi, G.; Marquaire, P.-M. Primary Mechanism of the Thermal Decomposition of Tricyclodecane. *J. Phys. Chem. A* **2006**, *110*, 11298–11314.
- (17) Park, S. H.; Kwon, C. H.; Kim, J.; Chun, B.-H.; Kang, J. W.; Han, J. S.; Jeong, B. H.; Kim, S. H. Thermal Stability and Isomerization Mechanism of Exo-Tetrahydrodicyclopentadiene: Experimental Study and Molecular Modeling. *Ind. Eng. Chem. Res.* **2010**, *49*, 8319–8324.
- (18) Rao, P. N.; Kunzru, D. Thermal Cracking of JP-10: Kinetics and Product Distribution. *J. Anal. Appl. Pyrolysis* **2006**, *76*, 154–160.
- (19) Xing, Y.; Fang, W.; Xie, W.; Guo, Y.; Lin, R. Thermal Cracking of JP-10 Under Pressure. *Ind. Eng. Chem. Res.* **2008**, *47*, 10034–10040.
- (20) Li, G.; Zhang, C.; Wei, H.; Xie, H.; Guo, Y.; Fang, W. Investigations on the Thermal Decomposition of JP-10/Iso-octane Binary Mixtures. *Fuel* **2016**, *163*, 148–156.
- (21) Davidson, D. F.; Horning, D. C.; Herbon, J. T.; Hanson, R. K. Shock Tube Measurements of JP-10 Ignition. *Proc. Combust. Inst.* **2000**, *28*, 1687–1692.
- (22) Morozov, A. N.; Mebel, A. M.; Kaiser, R. I. A Theoretical Study of Pyrolysis of Exo-Tetrahydrodicyclopentadiene and Its Primary and Secondary Unimolecular Decomposition Products. *J. Phys. Chem. A* **2018**, *122*, 4920–4934.
- (23) Striebich, R. C.; Lawrence, J. Thermal Decomposition of High-Energy Density Materials at High Pressure and Temperature. *J. Anal. Appl. Pyrolysis* **2003**, *70*, 339–352.
- (24) Johnson, S. E.; Davidson, D. F.; Hanson, R. K. Shock Tube/Laser Absorption Measurements of the Pyrolysis of JP-10 Fuel. *Combust. Flame* **2020**, *216*, 161–173.
- (25) Pan, Y.; Zhang, H.; Zhang, C.; Wang, H.; Jing, K.; Wang, L.; Zhang, X.; Liu, G. Supercritical Pyrolysis and Coking of JP-10 in Regenerative Cooling Channels. *Energy Fuels* **2020**, *34*, 1627–1638.
- (26) Huang, B.; Shrestha, U.; Davis, R. J.; Chelliah, H. K. Endothermic Pyrolysis of JP-10 With and Without Zeolite Catalyst for Hypersonic Applications. *AIAA J.* **2018**, *56*, 1616–1626.
- (27) Li, D.; Fang, W.; Wang, H.; Gao, C.; Zhang, R.; Cai, K. Gold/Oil Nanofluids Stabilized by a Gemini Surfactant and their Catalytic Property. *Ind. Eng. Chem. Res.* **2013**, *52*, 8109–8113.
- (28) Abrevaya, H. Unique Aspects of Mechanisms and Requirements for Zeolite Catalysis in Refining and Petrochemicals. *Zeolites in Industrial Separation and Catalysis*; Wiley, 2010; pp 403–478.
- (29) Rigutto, M. Cracking and hydrocracking. *Zeolites and Catalysis*; Wiley, 2010; pp 547–584.
- (30) Kokotailo, G. T.; Lawton, S. L.; Olson, D. H.; Meier, W. M. Structure of Synthetic Zeolite ZSM-5. *Nature* **1978**, *272*, 437–438.
- (31) Hoff, T. C.; Thilakaratne, R.; Gardner, D. W.; Brown, R. C.; Tessonier, J.-P. Thermal Stability of Aluminum-rich ZSM-5 Zeolites and Consequences on Aromatization Reactions. *J. Phys. Chem. C* **2016**, *120*, 20103–20113.
- (32) Auepattana-aumrung, C.; Márquez, V.; Wannakao, S.; Jongsomjit, B.; Panpranot, J.; Praserttham, P. Role of Al in Na-ZSM-5 Zeolite Structure on Catalyst Stability in Butene Cracking Reaction. *Sci. Rep.* **2020**, *10*, 13643.
- (33) Holzinger, J.; Beato, P.; Lundegeard, L. F.; Skibsted, J. Distribution of Aluminum over the Tetrahedral Sites in ZSM-5 Zeolites and Their Evolution After Steam Treatment. *J. Phys. Chem. C* **2018**, *122*, 15595–15613.
- (34) Xing, Y.; Li, D.; Xie, W.; Fang, W.; Guo, Y.; Lin, R. Catalytic Cracking of Tricyclo [5.2.1.02.6] Decane over HZSM-5 Molecular Sieves. *Fuel* **2010**, *89*, 1422–1428.
- (35) Tian, Y.; Qiu, Y.; Hou, X.; Wang, L.; Liu, G. Catalytic Cracking of JP-10 over HZSM-5 Nanosheets. *Energy Fuels* **2017**, *31*, 11987–11994.
- (36) Lu, C.; Liu, T.; Shi, Q.; Li, Q.; Xin, Y.; Zheng, L.; Zhang, Z. Plausibility of Potassium Ion-Exchanged ZSM-5 as Soot Combustion Catalysts. *Sci. Rep.* **2017**, *7*, 3300.
- (37) Song, G.; Chen, W.; Dang, P.; Yang, S.; Zhang, Y.; Wang, Y.; Xiao, R.; Ma, R.; Li, F. Synthesis and Characterization of Hierarchical ZSM-5 Zeolites with Outstanding Mesoporosity and Excellent Catalytic Properties. *Nanoscale Res. Lett.* **2018**, *13*, 364.
- (38) Dement'ev, K. I.; Palankov, T. A.; Kuznetsov, P. S.; Abramova, D. S.; Romazanova, D. A.; Makhin, D. Y.; Maksimov, A. L. Effect of Size Factor on the Activity of Zeolites in the Liquid-Phase Cracking of Hydrocarbons. *Pet. Chem.* **2020**, *60*, 30–38.
- (39) Tallon, J. L.; Buckley, R. G. Thermal Decomposition of the Zeolite Catalyst ZSM-5. *J. Phys. Chem.* **1987**, *91*, 1469–1475.
- (40) Olson, D. H.; Kokotailo, G. T.; Lawton, S. L.; Meier, W. M. Crystal Structure and Structure-Related Properties of ZSM-5. *J. Phys. Chem.* **1981**, *85*, 2238–2243.
- (41) The International Zeolite Association Homepage (The database for zeolite). https://asia.iza-structure.org/IZA-SC/material_tm.php?STC=MFI (accessed on May 6, 2021).
- (42) Xing, E.; Zhang, X.; Wang, L.; Mi, Z. Molecular Dimensions of Tetrahydrodicyclopentadiene isomers and Shape Selectivity of Zeolitic Catalysts. *Catal. Commun.* **2005**, *6*, 737–741.

- (43) Petrovic, I.; Navrotsky, A.; Davis, M. E.; Zones, S. I. Thermochemical Study of the Stability of Frameworks in High Silica Zeolites. *Chem. Mater.* **1993**, *5*, 1805–1813.
- (44) Guisnet, M.; Costa, L.; Ribeiro, F. R. Prevention of Zeolite Deactivation by Coking. *J. Mol. Catal. A: Chem.* **2009**, *305*, 69–83.
- (45) Guisnet, M.; Magnoux, P. Organic Chemistry of Coke Formation. *Appl. Catal., A* **2001**, *212*, 83–96.
- (46) Guisnet, M.; Magnoux, P. Coking and Deactivation of Zeolites: Influence of the Pore Structure. *Appl. Catal.* **1989**, *54*, 1–27.
- (47) Brotton, S. J.; Malek, M. J.; Anderson, S. L.; Kaiser, R. I. Effects of Acetonitrile-Assisted Ball-Milled Aluminum Nanoparticles on the Ignition of Acoustically Levitated Exo-Tetrahydrodicyclopentadiene (JP-10) Droplets. *Chem. Phys. Lett.* **2020**, *754*, 137679.
- (48) Lucas, M.; Brotton, S. J.; Min, A.; Pantoya, M. L.; Kaiser, R. I. Oxidation of Levitated Exo-Tetrahydrodicyclopentadiene Droplets Doped with Aluminum Nanoparticles. *J. Phys. Chem. Lett.* **2019**, *10*, 5756–5763.
- (49) Lucas, M.; Brotton, S. J.; Min, A.; Woodruff, C.; Pantoya, M. L.; Kaiser, R. I. Effects of Size and Prestressing of Aluminum Particles on the Oxidation of Levitated Exo-Tetrahydrodicyclopentadiene Droplets. *J. Phys. Chem. A* **2020**, *124*, 1489–1507.
- (50) Guerrieri, P. M.; Jacob, R. J.; DeLisio, J. B.; Rehwoldt, M. C.; Zachariah, M. R. Stabilized Microparticle Aggregates of Oxygen-Containing Nanoparticles in Kerosene for Enhanced Droplet Combustion. *Combust. Flame* **2018**, *187*, 77–86.
- (51) Xiu-Tian-Feng, E.; Pan, L.; Wang, F.; Wang, L.; Zhang, X.; Zou, J.-J. Al-Nanoparticle-Containing Nanofluid Fuel: Synthesis, Stability, Properties, and Propulsion Performance. *Ind. Eng. Chem. Res.* **2016**, *55*, 2738–2745.
- (52) Xiu-Tian-Feng, E.; Zhi, X.; Zhang, X.; Wang, L.; Xu, S.; Zou, J. J. Ignition and Combustion Performances of High-Energy-Density Jet Fuels Catalyzed by Pt and Pd Nanoparticles. *Energy Fuels* **2018**, *32*, 2163–2169.
- (53) Javed, I.; Baek, S. W.; Waheed, K. Autoignition and Combustion Characteristics of Heptane Droplets with the Addition of Aluminium Nanoparticles at Elevated Temperatures. *Combust. Flame* **2015**, *162*, 191–206.
- (54) Liu, L.; Zhang, Q.; Shen, S.; Li, D.; Lian, Z.; Wang, Y. Evaluation of Detonation Characteristics of Aluminum/JP-10/Air Mixtures at Stoichiometric Concentrations. *Fuel* **2016**, *169*, 41–49.
- (55) Luo, Y.; Xu, X.; Zou, J.-J.; Zhang, X. Combustion of JP-10-Based Slurry with Nanosized Aluminum additives. *J. Propul. Power* **2016**, *32*, 1167–1177.
- (56) E, X.-T. -F.; Zhang, L.; Wang, F.; Zhang, X.; Zou, J.-J. Synthesis of Aluminum Nanoparticles as Additive to Enhance Ignition and Combustion of High Energy Density Fuels. *Front. Chem. Sci. Eng.* **2018**, *12*, 358–366.
- (57) Sundaram, D. S.; Yang, V.; Zarko, V. E. Combustion of Nano Aluminum Particles (Review). *Combust., Explos. Shock Waves* **2015**, *51*, 173–196.
- (58) Brotton, S. J.; Kaiser, R. I. Novel High-Temperature and Pressure-Compatible Ultrasonic Levitator Apparatus Coupled to Raman and Fourier Transform Infrared Spectrometers. *Rev. Sci. Instrum.* **2013**, *84*, 055114.
- (59) Brotton, S. J.; Kaiser, R. I. In situ Raman Spectroscopic Study of Gypsum ($\text{CaSO}_4 \cdot 2\text{H}_2\text{O}$) and Epsomite ($\text{MgSO}_4 \cdot 7\text{H}_2\text{O}$) Dehydration Utilizing an Ultrasonic Levitator. *J. Phys. Chem. Lett.* **2013**, *4*, 669–673.
- (60) Brotton, S. J.; Lucas, M.; Jensen, T. N.; Anderson, S. L.; Kaiser, R. I. Spectroscopic Study on the Intermediates and Reaction Rates in the Oxidation of Levitated Droplets of Energetic Ionic Liquids by Nitrogen Dioxide. *J. Phys. Chem. A* **2018**, *122*, 7351–7377.
- (61) McCrary, P. D.; Beasley, P. A.; Cojocar, O. A.; Schneider, S.; Hawkins, T. W.; Perez, J. P. L.; McMahon, B. W.; Pfeil, M.; Boatz, J. A.; Anderson, S. L.; Son, S. F.; Rogers, R. D. Hypergolic Ionic Liquids to Mill, Suspend, and Ignite Boron Nanoparticles. *Chem. Commun.* **2012**, *48*, 4311–4313.
- (62) Vankoningsveld, H.; Jansen, J.; Vanbekkum, H. The Monoclinic Framework Structure of Zeolite H-ZSM-5. Comparison with the Orthorhombic Framework of As-synthesized ZSM-5. *Zeolites* **1990**, *10*, 235–242.
- (63) Lee, C. P.; Wang, T. G. Acoustic Radiation Force on a Heated Sphere Including Effects of Heat Transfer and Acoustic Streaming. *J. Acoust. Soc. Am.* **1988**, *83*, 1324–1331.
- (64) Gaydon, A. *The Spectroscopy of Flames*; Springer Science & Business Media, 2012.
- (65) Hein, I. D. The Database for Excitation-Emission Spectra (EES) in Combustion Research. http://www.combustion-database.com/AES/aes_home.htm (accessed on March 7, 2021).
- (66) Linstrom, P. J.; Mallard, W. G. The NIST Chemistry WebBook: A Chemical Data Resource on the Internet†. *J. Chem. Eng. Data* **2001**, *46*, 1059–1063.
- (67) Gordon, I. E.; Rothman, L. S.; Hill, C.; Kochanov, R. V.; Tan, Y.; Bernath, P. F.; Birk, M.; Boudon, V.; Campargue, A.; Chance, K. V.; Drouin, B. J.; Flaud, J.-M.; Gamache, R. R.; Hodges, J. T.; Jacquemart, D.; Perevalov, V. I.; Perrin, A.; Shine, K. P.; Smith, M.-A. H.; Tennyson, J.; Toon, G. C.; Tran, H.; Tyuterev, V. G.; Barbe, A.; Császár, A. G.; Devi, V. M.; Furtenbacher, T.; Harrison, J. J.; Hartmann, J.-M.; Jolly, A.; Johnson, T. J.; Karman, T.; Kleiner, I.; Kyuberis, A. A.; Loos, J.; Lyulin, O. M.; Massie, S. T.; Mikhailenko, S. N.; Moazzen-Ahmadi, N.; Müller, H. S. P.; Naumenko, O. V.; Nikitin, A. V.; Polyansky, O. L.; Rey, M.; Rotger, M.; Sharpe, S. W.; Sung, K.; Starikova, E.; Tashkun, S. A.; Auwera, J. V.; Wagner, G.; Wilzewski, J.; Wcislo, P.; Yu, S.; Zak, E. J. The HITRAN2016 Molecular Spectroscopic Database. *J. Quant. Spectrosc. Radiat. Transfer* **2017**, *203*, 3–69.
- (68) Sansonetti, J. E. Wavelengths, Transition Probabilities, and Energy Levels for the Spectra of Potassium (KI through K XIX). *J. Phys. Chem. Ref. Data* **2008**, *37*, 7–96.
- (69) Tennyson, J.; Bernath, P. F.; Brown, L. R.; Campargue, A.; Császár, A. G.; Daumont, L.; Gamache, R. R.; Hodges, J. T.; Naumenko, O. V.; Polyansky, O. L.; et al. IUPAC Critical Evaluation of the Rotational–Vibrational Spectra of Water Vapor, Part III: Energy Levels and Transition Wavenumbers for H_2^{16}O . *J. Quant. Spectrosc. Radiat. Transfer* **2013**, *117*, 29–58.
- (70) Rumbles, G.; Lee, E. K. C.; Valentini, J. J. Laser-Induced Fluorescence from the Predissociating Formyl Radical. Part 2.— Analysis of Dispersed Emission from the \tilde{A} – \tilde{X} Transition. *J. Chem. Soc., Faraday Trans.* **1990**, *86*, 3837–3841.
- (71) Miller, C. E.; Brown, L. R. Near Infrared Spectroscopy of Carbon Dioxide I. $^{16}\text{O}^{12}\text{C}^{16}\text{O}$ line positions. *J. Mol. Spectrosc.* **2004**, *228*, 329–354.
- (72) VPL molecular spectroscopic database. <http://vpl.astro.washington.edu/spectra/> (accessed on March 9, 2021).
- (73) Dong, X.; Shaikh, S.; Vittenet, J. R.; Wang, J.; Liu, Z.; Bhatte, K. D.; Ali, O.; Xu, W.; Osorio, I.; Saih, Y.; Basset, J.-M.; Ali, S. A.; Han, Y. Fine Tuning the Diffusion Length in Hierarchical ZSM-5 to Maximize the Yield of Propylene in Catalytic Cracking of Hydrocarbons. *ACS Sustainable Chem. Eng.* **2018**, *6*, 15832–15840.
- (74) Krishnamoorthy, A.; Varghese, S. Role of Surfactants on the Stability of Nano-Zinc Oxide Dispersions. *Part. Sci. Technol.* **2017**, *35*, 67–70.
- (75) Porter, R. P.; Clark, A. H.; Kaskan, W. E.; Browne, W. E. A study of hydrocarbon flames. *Symposium (International) on Combustion*; Elsevier, 1967; Vol. 11, pp 907–917.